Article

Phase-Sensitive Vibrational Sum and Difference Frequency-Generation Spectroscopy Enabling Nanometer-Depth Profiling at Interfaces

Vasileios Balos, Tobias Garling, Alvaro Diaz Duque, Ben John, Martin Wolf, and Martin Thämer*

Read Online

ACCESS | Metrics & More | Article Recommendations | SI Supporting Information

ABSTRACT: The unique physical and chemical properties of interfaces are governed by a finite depth that describes the transition from the topmost atomic layer to the properties of the bulk material. Thus, understanding the physical nature of interfaces requires detailed insight into the different structures, chemical compositions, and physical processes that form this interfacial region. Such insight has traditionally been difficult to obtain from experiments, as it requires a combination of structural and chemical sensitivity with spatial depth resolution on the nanometer scale. In this contribution, we present a vibrational spectroscopic approach that can overcome these limitations. By combining phase-sensitive sum and difference frequency-generation (SFG and DFG, respectively) spectroscopy and by selectively determining different nonlinear interaction pathways, we can extract precise depth information and correlate these to specific vibrationally resonant modes of interfacial species. We detail the mathematical framework behind this approach and demonstrate the performance of this technique in two sets of experiments on selected model samples. An analysis of the results shows an almost perfect match between experiment and theory, confirming the practicability of the proposed concept under realistic experimental conditions. Furthermore, in measurements with self-assembled monolayers of different chain lengths, we analyze the spatial accuracy of the technique and find that the precision can even reach the sub-nanometer regime. We also discuss the implications and the information content of such depth-sensitive measurements and show that the concept is very general and goes beyond the analysis of the depth profiles. The presented SFG/DFG technique offers new perspectives for spectroscopic investigations of interfaces in various material systems by providing access to fundamental observables that have so far been inaccessible by experiments. Here, we set the theoretical and experimental basis for such future investigations.
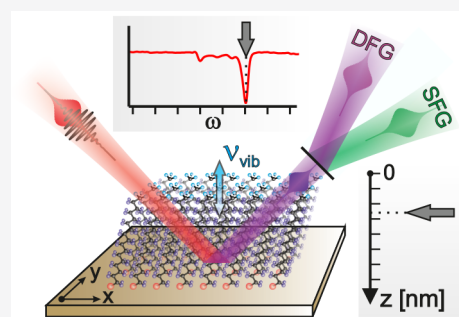
INTRODUCTION

Interfaces between different materials are omnipresent in nature, and their unique physical and chemical properties enable a variety of processes that exclusively happen at these exceptional and spatially delimited places in matter. Such interfacial processes often include molecular species that play a key role in numerous fields; for example, they are the bases of many fundamental functions in biology[1−4] and govern a significant portion of atmospheric (e.g., aerosol) chemistry.[5−7] Besides their importance in nature, the special properties of molecular interfaces are also exploited in various scientific fields and important industrial applications such as electrochemistry[8−10] (e.g., for energy storage solutions), heterogeneous catalysis,[11,12] colloid science,[13,14] etc. Triggered by this outstanding role of interfaces, the scientific community has seen an ever-increasing interest to obtain a detailed understanding of their complex physical nature. However, despite decades of intensive research, our microscopic (molecular-level) understanding of the fundamental properties of many interfacial systems is still rather limited and largely based on results from theory.

One reason for the difficulty to experimentally unravel the full picture of the physics of interfaces is related to the fact that the interface in various systems cannot be represented by a simple two-dimensional interfacial plane.[15−17] The presence of an interface may rather impact the physical and chemical properties in the adjoining materials over many molecular/atomic layers forming a three-dimensional interfacial region. Taking as example liquid interfaces, the spatial extension of the interfacial region can involve various effects, such as preferential molecular orientations that translate into the bulk phases, depth-dependent chemical compositions, electric fields that are generated by surface potentials, modified intermolecular interactions or more general, depth-dependent structural motifs and molecular dynamics.[18−20] All these effects
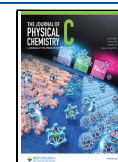
contribute to the physics of the interface and participate in interfacial processes. Therefore, in order to attain a true understanding of the fundamental physics of such interfaces it is not sufficient to experimentally characterize only the topmost molecular/atomic layer, but an experimental probe is needed that can address these interfacial depth profiles, with combined structural and chemical sensitivity and spatial resolution perpendicular to the phase boundary.

Experimental investigations of interfaces have been performed using various surface-sensitive techniques using X-rays, electrons, or light as a probe. Examples include X-ray-based techniques, like X-ray photoelectron spectroscopy (XPS),[21] X-ray scattering and diffraction,[22] and extended X-ray absorption fine structure (EXAFS),[23] electron-beam-based techniques, such as low energy electron diffraction (LEED)[24] or Auger-electron spectroscopy (AES),[25,26] but also coherent optical techniques such as second harmonic generation (SHG) or sum frequency generation (SFG) spectroscopy.[27−29] All these methods are well-established and powerful analytical tools for the characterization of interfaces; however, for the investigation of molecular interfaces vibrational SFG spectroscopy has proven particularly useful. The prominent role of SFG in such studies is based on its sensitivity to molecular vibrations, which allows one to identify interfacial molecular species and analyze intermolecular structures and interactions.

Overall, with all the methods shown above, a large toolbox of complementary experimental techniques is available allowing for a very profound characterization of interfaces. However, performing such studies with the desired depth resolution in a nondestructive manner has been proven to be a difficult experimental task and has been a longstanding challenge in interface science.

Conceptually, all these techniques probe a specific volume around the phase boundary that is defined by some, more or less known, material constants, for example, for XPS by the electron mean free path length inside the sample. To decompose the detected signals into the different contributions from the various depths, additional experimental information is needed. Over the last decades several technical advancements have been developed that can yield precise spatial depth resolution. The required additional information is thereby obtained, for example, by angular resolved measurements (e.g., angle-resolved XPS),[30,31] by an analysis of spatial and/or spectral interference patterns (e.g., grazing incidence XRD),[32] or by the use of an additional interferometric stimulus with high spatial specificity as in X-ray standing-wave techniques.[33−36] These technical developments represent major experimental achievements for interfacial studies because they yield the desired access to the interfacial depth profiles. Such studies have provided important new insights into the physics of interfacial regions of various materials, but for the investigation of molecular interfaces it would be highly desirable to perform similar depth-resolved studies with a vibrational (SFG) probe. However, such an advanced SFG technique has so far not been available.

In this publication we present a novel spectroscopic approach that adds spatial depth resolution, on the nanometer scale, to vibrationally resonant nonlinear spectra from the interfacial region. It is based on a combination of phase-sensitive sum and difference generation spectroscopies (SFG and DFG, respectively) and allows us to correlate obtained depth profiles to specific molecular species and their intermolecular structures by probing their characteristic nonlinear vibrational spectra. In the following two sections we present the concept of this technique along with the underlying mathematical framework. In the result part we show measurements on several selected model samples that demonstrate the experimental applicability of the presented method, followed by a detailed experimental analysis of its spatial accuracy. Finally, we discuss the information content and the limitations of such depth-resolved experiments. This work sets the basis for accurately performing depth-resolved molecular spectroscopic studies on relevant (e.g., liquid) interfaces and opens the perspective of obtaining a better understanding of the fundamental physics governing such systems.

Sum Frequency Generation Spectroscopy. Vibrational second-order spectroscopic methods such as SFG and DFG[37−43] are based on the effect of nonlinear frequency mixing in a sample. By overlapping two intense laser beams, one in the infrared (E^a) and the other typically in the visible frequency range (E^b), a nonlinear polarization is induced in the sample, which gives rise to the emission of signals at the sum and difference frequency (E^c), which can be detected and analyzed. The involved frequencies are usually chosen such that the visible up-conversion beam is far from any resonance, while the infrared beam excites specific vibrations of interest in the sample. The frequency-mixing process can be described by the following eq 1.

$$E^c(\omega^c) \sim \chi_{eff}^{(2)}(\omega^c = \omega^a + \omega^b) \cdot E^b(\omega^b) \cdot E^a(\omega^a) \tag{1}$$

The quantity that connects the three fields and, in particular, their frequencies ω is the effective second-order susceptibility $\chi_{eff}^{(2)}$, which contains the desired spectroscopic information and which is the key quantity that is typically determined in phase-sensitive nonlinear experiments.[44−49] A measurement from a sample of interest is thereby normalized to a second measurement of a reference sample with a known susceptibility.[50,51] $\chi_{eff}^{(2)}$ is, in general, a complex quantity, and its spectrum reports on vibrational resonances and the orientation of the corresponding functional groups, forming peaks or dips in the spectra.[52−57]

One important advantage of this spectroscopy, when compared to other mentioned techniques, arises from the fact that $\chi_{eff}^{(2)}$ is sensitive to symmetry. In sample regions possessing centro-symmetry, $\chi_{eff}^{(2)}$ is zero under the electric dipole approximation, and consequently no signal is generated. This is true, for example, for the bulk in most materials. In the entire (extended) interfacial region, however, the centro-symmetry is necessarily broken, and second-order signals can be generated because all the interfacial effects described earlier have a clear directionality toward the phase boundary. Hence, second-order spectroscopies naturally probe the entire region of interest and therefore fulfill an essential requirement for the intended investigations.

Apart from this specificity to the interfacial region, another crucial aspect of these techniques is that the resulting signals also contain information on their spatial origin along the surface normal.[42] As illustrated in Figure 1, a nonlinear signal generated in some depth below the phase boundary (P_1) acquires a phase shift compared to a signal generated at the phase boundary (P_0), due to the involved different optical path lengths.[58,59] In the given example the resulting phase shift $\phi(z)$ amounts to
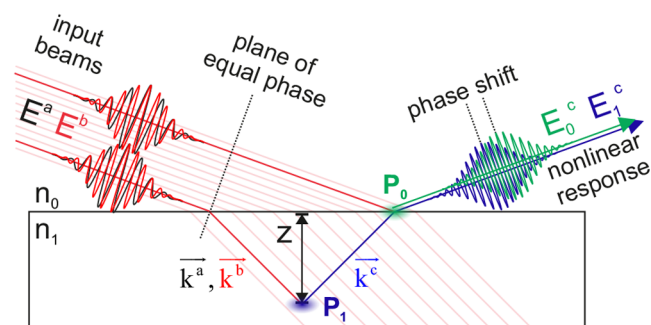
$$\phi(z) = \Delta k_z \cdot z \tag{2}$$

Figure 1. Optical pathways for nonlinear radiation sources P_0 and P_1 with different depth coordinates.

where Δk_z is the z-component of the wave vector mismatch between the incident (k_a and k_b) and the generated light waves k_c.[43]

$$\Delta k_z = k_z^a + k_z^b - k_z^c \tag{3}$$

This phase shift obviously modifies the shape of the resulting nonlinear spectra. We can account for this effect by defining a local susceptibility $\chi_{loc}^{(2)}$ that describes the intrinsic nonlinear response of the sample in a plane located at the depth z. Including the propagation-induced phase shift $\phi(z)$ we obtain for the measured effective susceptibility the following expression

$$\chi_{eff}^{(2)} = \chi_{loc}^{(2)} \cdot e^{i\phi(z)} = |\chi_{loc}^{(2)}| \cdot e^{i(\phi_R + \phi(z))} \tag{4}$$

where ϕ_R is the intrinsic phase of the local susceptibility.

eqs 2 and 4 are accurate for samples with a spatially well-defined signal source that is located at some position z. To describe the more general case of a sample with an extended interfacial region, the equations must be slightly modified. In such systems the contribution to a nonlinear signal generated from a particular species of interest will typically follow some distribution in z that decays to zero toward the bulk. The overall signal will then be composed of the sum of these contributions. Mathematically this means that we need to integrate all the individual contributions in z to calculate the effective susceptibility. As a result of such an integration we also obtain a propagation-induced (effective) phase shift $\phi(z')$ only that now it reports on the length-scale on which the contribution decays (z') rather than on a well-defined z-coordinate. Furthermore, in this case the summation also influences the amplitude of the overall response. This can be accounted for by including the amplitude scaling factor $C(z')$. Therefore, we can express the effective susceptibility for this general case with the following equation.

$$\chi_{eff}^{(2)} = |\chi_{loc}^{(2)}| \cdot C(z') \cdot e^{i(\phi_R + \phi(z'))} \tag{5}$$

The exact expressions for $\phi(z')$ and $C(z')$ depend on the functional form of the signal decay toward the bulk. In many cases, however, it will be a good approximation to assume an exponential decay with the decay constant z'. The integration then yields for the propagation induced phase shift[58,60]

$$\phi(z') = \arctan(\Delta k_z \cdot z') \tag{6}$$

and for the scaling factor $C(z')$

$$C(z') = 1/\sqrt{((1/z')^2 + (\Delta k_z)^2)} \tag{7}$$

Note that the scaling factor is always real, implying that it does not contribute to the phase of the overall response. From this theoretical description of the nonlinear sample response, we see that the desired depth information is indeed encoded in the measured spectra or more precisely in the value of $\phi(z)$. On the basis of the equations shown above we can extract this information in a straightforward manner from the propagation-induced phase shift. Furthermore, with typical values for Δk_z in the order of 1/50 nm the expected phase shift in $\phi(z)$ amounts to ~1 °ree per nanometer in depth. Since a phase accuracy on the order of 1° can be achieved using state-of-the-art nonlinear spectrometers,[50,55,57,61] it should, in principle, be possible to obtain a depth resolution on the single-digit nanometer scale.

The main challenge to obtain the desired depth information from the nonlinear spectra is, however, the precise determination of $\phi(z)$. With phase-sensitive SFG spectroscopy we can determine with high accuracy the spectral phase of $\chi_{eff}^{(2)}$, but in order to determine $\phi(z)$ we need to precisely know the intrinsic phase ϕ_R of the local susceptibility $\chi_{loc}^{(2)}$ (see eqs 4 and 5). The latter is known in the case of fully off-resonant studies, where $\chi_{loc}^{(2)}$ becomes entirely real with a phase ϕ_R of 0 or 180°. As previously demonstrated[60,62,63] such experiments can indeed yield information about the depth profile. However, with off-resonant studies we do not obtain any spectral information in the interfacial region that we could correlate with the depth information. In contrast, when probing characteristic vibrational resonances, we can identify and distinguish different structures or species of interest in the interfacial region, but at the cost that ϕ_R now becomes highly dependent on the infrared frequency. Without prior knowledge of the exact locations and line shapes of the involved resonant modes (which is typically not available) it is impossible to predict the spectral shape of ϕ_R. Using traditional phase-sensitive SFG spectroscopy the desired quantity $\phi(z)$ therefore remains buried in the measured data without a realistic chance to extract it. As shown in the following this challenge can be overcome by simultaneously measuring phase-sensitive SFG and DFG spectra.

Combined SFG/DFG Spectroscopy. To understand this concept, we need to analyze the different nonlinear interaction pathways that compose the overall SFG and DFG responses in a nonlinear experiment. $\chi_{eff}^{(2)}$ connects all involved frequencies ω^a, ω^b, and ω^c, and since these frequencies must obey the frequency relation $\omega^c = \omega^a + \omega^b$ only two of these parameters can be freely chosen. These two free parameters (for convenience we use here ω^c and ω^a) span a two-dimensional surface in frequency space (see Figure 2). The frequencies can thereby take positive and negative values forming four quadrants (A−D). With the incident laser beams $E(\omega_1^a)$ and $E(\omega_2^b)$ we obtain responses in all four quadrants, two representing the SFG response and its complex conjugate (red shaded areas) and the other two the DFG response and its complex conjugate (blue shaded areas). The lower indices (1, 2, 3, and 4) thereby signify different frequency values, and the upper indices (a, b, and c) mark the frequency axes corresponding to the respective interacting field. If the SFG and DFG signals are both measured with phase resolution, all four pathways are individually obtained, but due to their mutual relation only two (one SFG and one DFG pathway) carry nontrivial spectroscopic information. In the following we will concentrate on the two pathways A and B, which correspond to $\chi_{eff}^{(2)}(\omega_1^a, \omega_3^c)$ and $\chi_{eff}^{(2)}(\omega_1^a, -\omega_4^c)$, respectively.
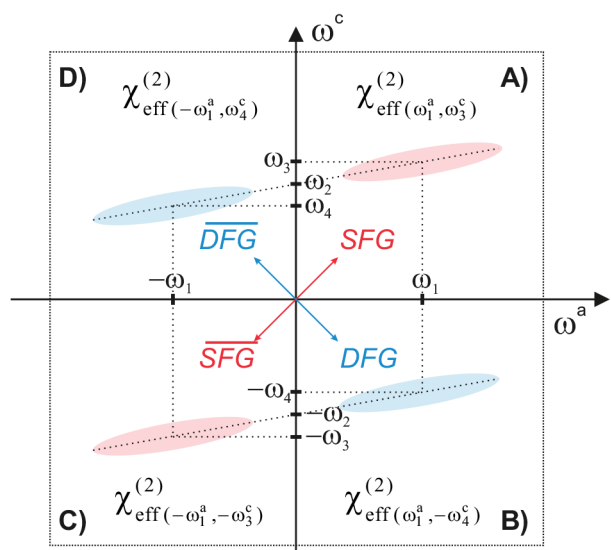
Figure 2. Two-dimensional representation of $\chi_{\text{eff}}^{(2)}$ as a function of the frequencies of the infrared (ω^a) and the nonlinear signal (ω^c). The nonlinear interaction gives rise to SFG (red shaded area) and DFG (blue shaded area) signals. Frequency axis of infrared beam ω^a with the center frequency $\pm\omega_1$; frequency axis of nonlinear signal ω^c (different scaling) with the center frequencies $\pm\omega_3$ (SFG) and $\pm\omega_4$ (DFG).

Implementing these frequency arguments into eq 5 we obtain the following expressions.

$$\chi_{\text{eff}}^{(2)}(\omega_1^a, \omega_3^c) = \chi_{\text{loc}}^{(2)}(\omega_3^c = \omega_1^a + \omega_2^b) \cdot C^{\text{SFG}}(z') \cdot e^{(i\phi^{\text{SFG}}(z'))} \tag{8}$$

$$\chi_{\text{eff}}^{(2)}(\omega_1^a, -\omega_4^c) = \chi_{\text{loc}}^{(2)}(-\omega_4^c$$
$$= \omega_1^a - \omega_2^b) \cdot C^{\text{DFG}}(z') \cdot e^{(i\phi^{\text{DFG}}(z'))} \tag{9}$$

In order to compare these two responses, we need to analyze how the change in the frequency arguments affects the resulting effective susceptibility.

In a first step we analyze the two local susceptibilities $\chi_{\text{loc}}^{(2)}(\omega_3^c = \omega_1^a + \omega_2^b)$ and $\chi_{\text{loc}}^{(2)}(-\omega_4^c = \omega_1^a - \omega_2^b)$. Comparing the two frequency arguments, we see that the vibrational frequencies ω_1 appear in both expressions with the same sign. This intuitively suggests that the presence of a vibrational resonance affects phases and amplitudes of the two local susceptibilities in the same way. Furthermore, if the other involved (visible) frequencies (ω_2, ω_3, and ω_4) are tuned to be far off-resonance with any transition in the investigated sample, the local susceptibilities should be fairly independent of their exact values and, in particular, their signs. From these rationalizing arguments we can conclude that the two local susceptibilities shown above should be equal. In fact, the equality of the two quantities under the conditions mentioned above can mathematically be derived from general symmetry considerations of the susceptibility tensors (see the Supporting Informaton). This finding implies that also the intrinsic phases ϕ_R are equal for the selected SFG and DFG pathways as long as the involved (visible) frequencies are far off-resonance.

We now turn to the remaining factors ($C(z')$ and $\phi(z')$) in the expressions of effective susceptibilities in eqs 8 and 9, and here the situation is different. These factors depend on the wavevector mismatch Δk_z. The phase-matching conditions for

pathways A and B in Figure 2 are $\overrightarrow{k^c(\omega_3)} = \overrightarrow{k^a(\omega_1)} + \overrightarrow{k^b(\omega_2)}$ and $-\overrightarrow{k^c(\omega_4)} = \overrightarrow{k^a(\omega_1)} - \overrightarrow{k^b(\omega_2)}$, respectively. Considering reflection geometry, we obtain for the corresponding wave-vector mismatches

$$\Delta k_z^{\text{SFG}} = |k_z^a(\omega_1)| + |k_z^b(\omega_2)| + |k_z^c(\omega_3)| > 0 \tag{10}$$

and

$$\Delta k_z^{\text{DFG}} = |k_z^a(\omega_1)| - |k_z^b(\omega_2)| - |k_z^c(\omega_4)| < 0 \tag{11}$$

We see that Δk_z^{SFG} and Δk_z^{DFG} differ in their absolute values, but more importantly they have opposite signs. While the deviating magnitudes lead to different values for the scaling factors $C(z')$, the sign flip directly translates into opposite signs in the propagation phases $\phi(z')$ for the SFG and DFG pathways (see eq 6). If we implement these properties of $\chi_{\text{loc}}^{(2)}$ and $\phi(z')$ for the SFG and DFG pathways into eqs 8 and 9, we obtain the following expressions for the effective susceptibilities.

$$\chi_{\text{eff}}^{(2)}(\omega_1^a, \omega_3^c) = |\chi_{\text{loc}}^{(2)}| \cdot C^{\text{SFG}}(z) \cdot e^{i(\phi_R + \arctan(|\Delta k_z^{\text{SFG}}| \cdot z'))} \tag{12}$$

$$\chi_{\text{eff}}^{(2)}(\omega_1^a, -\omega_4^c) = |\chi_{\text{loc}}^{(2)}| \cdot C^{\text{DFG}}(z) \cdot e^{i(\phi_R - \arctan(|\Delta k_z^{\text{DFG}}| \cdot z'))} \tag{13}$$

eqs 12 and 13 show that the phase of the resonant local susceptibility ϕ_R enters both equations with the same sign, whereas the propagation phase $\phi(z')$ shows a sign flip. This property makes ϕ_R and $\phi(z')$ now separable. We can precisely determine the propagation phase $\phi(z')$, for example, by simply extracting the phase difference between the measured SFG and DFG spectra because ϕ_R cancels out in this expression. That way we get direct access to the desired depth parameter z' independent from the shape of the vibrational spectrum of the surface layer. Furthermore, with such measurements we also obtain this vibrational information as it is present in the resulting SFG and DFG spectra. Overall, this section shows theoretically that the proper combination of phase-sensitive SFG and DFG spectroscopy allows us to simultaneously obtain, indeed, both spectral and spatial information from an interface and to correlate them. Note, the comparison of the two selected pathways (SFG and DFG) presented above is performed using (as example) the equations that describe the case of spatially extended contributions with an exponential signal decay in z. For the case of a spatially well-defined signal source (eq 4) the derivation is similar and yields the same qualitative results.

■ EXPERIMENTAL SECTION

With this theoretical description of the presented concept in hand we now focus on its experimental realization. Performing such depth-resolved experiments is far from trivial, since it requires the measurement of phase-sensitive SFG and DFG spectra with very high accuracy. However, the nonlinear signals generated in interfacial regions are typically very weak, and the phases and spectra of the involved laser pulses tend to drift with time. Furthermore, to extract the $\chi_{\text{eff}}^{(2)}$ from a measured spectrum we need an equally precise reference measurement using a sample with known $\chi_{\text{eff}}^{(2)}$ that is measured under the exact same experimental conditions.[57,64] To tackle these challenges we use, for the studies presented here, a newly developed spectrometer that allows us to simultaneously
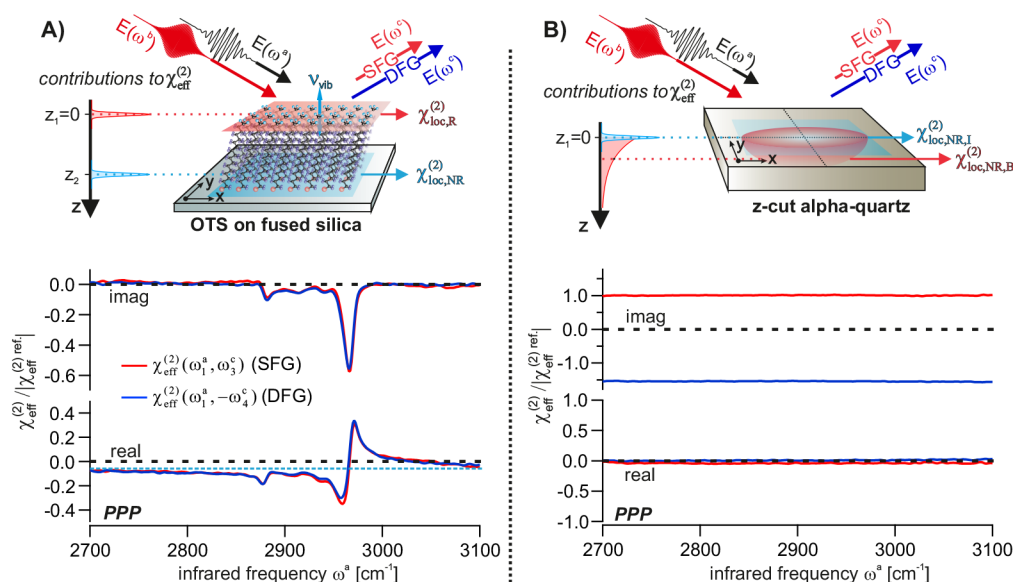
Figure 3. (A) SFG/DFG measurement of a self-assembled monolayer of OTS on fused silica and (B) SFG/DFG measurement of a z-cut α-quartz crystal. The measurement is taken with a PPP polarization scheme (all interacting fields are p-polarized with respect to the surface) and an angle of incidence of 70°. The wavelength of the up-conversion pulse is 690 nm. All amplitudes are normalized to the amplitude of the SFG response from z-cut quartz.

measure phase-sensitive SFG and DFG spectra. The data acquisition is based on a broadband time-domain approach using a unique, homemade nonlinear interferometer, which has been described in detail elsewhere.[57] The interferometer generates a single output beam that is sent to the sample area. It contains sequences of infrared, visible up-conversion, and local oscillator pulses (SFG and DFG) with tunable time delays. It is operated by two input laser beams (broadband infrared and broadband visible) generated from two commercial OPAs that are pumped by a commercial Ti:Sa amplified laser system (35 fs pulses at 800 nm and a repetition rate of 1 kHz).

The entire spectroscopic setup employs a fully collinear beam geometry and is equipped with a shot-to-shot referencing capability. Using a vibrating mirror behind the interferometer that oscillates at half the laser repetition rate we alternately measure the nonlinear responses of the sample and a reference crystal. This allows for efficient cancellation of drifts in phase and spectral shape.[57] The nonlinear signals (SFG and DFG) that are generated by the sample/reference interfere with the corresponding reflected local oscillator pulses get separated by a dichroic mirror and are independently detected by two pairs of commercial avalanche photodiodes in a balanced detection scheme.[57] The interferometric data are obtained by modifying the time delays in the pulse sequences using a fast-scanning approach, quite similar to the technique applied in regular Fourier transform infrared (FTIR) spectrometers. Analogously to this linear counterpart, the final spectra are then obtained by a Fourier transformation of the resulting interferograms and correction for the reference data. However, instead of one linear vibrational spectrum (as in FTIR) we obtain with our spectrometer for each scan four nonlinear spectra, that is, SFG and DFG for both sample and reference.

As described above the local oscillator pulses are created first and are reflected from the sample together with the generated nonlinear signals. This approach has two important advantages: First, that way fluctuations between the local oscillator

and signal phases induced by vibrating or drifting sample surfaces (e.g., in the case of liquid samples) are reduced and second, this beam geometry yields a natural spatial reference point ($z = 0$) for depth-resolved measurements, which is defined by the plane of (linear) reflection of the local oscillator pulses. More details about the experimental setup can be found in refs 57 and 64.

RESULTS AND DISCUSSION

Proof of Principle Measurements. The presented theoretical concept for depth-resolved interfacial studies is based on two crucial cornerstones: (i) the local susceptibilities are equal for the SFG and DFG pathways even in the presence of vibrationally resonant transitions in the sample (as long as all other light−matter interactions with the sample are purely nonresonant) and (ii) signals that originate from some depth with respect to the surface cause phase shifts with opposite directions in the measured *effective* susceptibilities for the SFG and DFG pathways. In other words, when the origin of the nonlinear signal is located at $z = 0$ we should always observe equal SFG and DFG spectra, whereas for signals with $z \neq 0$ the spectra should deviate. Although already shown theoretically, we will verify the validity of these fundamental aspects of the SFG/DFG concept experimentally using two well-defined model systems. In a first step we derive the mathematical form of the expected SFG/DFG responses for the two samples, and subsequently we compare the predictions to actual measurements.

The first test sample is a fused silica (FS) substrate that is functionalized with an octadecyltrichlorosilane (OTS) self-assembled monolayer (SAM). Such SAMs have been extensively studied using SFG spectroscopy[65−70] and yield relatively strong resonance peaks in the frequency range of the C−H stretching vibration (2800−3000 cm^{-1}). Neither the molecular monolayer nor the substrate possess any resonant electronic transitions in the visible range. This makes the sample a suitable model system to test relation (i).

There are two distinct contributions to the nonlinear signals. One is the resonant contribution of the molecular monolayer, and the other is the nonresonant contribution from the SAM-FS interface (see Figure 3A). Because of the close match of the refractive indices of the organic monolayer and the FS substrate (both with values of ~1.46[71,72]) the local oscillator is almost entirely reflected at the topmost interface (SAM/air). Therefore, this interface defines our reference plane ($z = 0$) within our depth-resolved measurements. Because of the symmetry selection rules of the second-order process, the resonant nonlinear response of the SAM originates almost exclusively from the terminal methyl groups[73,74] forming a spatially well-defined signal source at $z_1 = 0$ ($\chi^{(2)}_{\text{loc,R}}$, see Figure 3A). The comparatively weak nonresonant signal from the internal interface is spatially also well-defined but located at $z = z_2$ ($\chi^{(2)}_{\text{loc,NR}}$ in Figure 3A). The overall measured effective susceptibility $\chi^{(2)}_{\text{eff}}$ is simply the sum of the individual contributions. Including the corresponding phase propagation factors to account for the different depths we obtain for the SFG and DFG responses of our sample the following expressions.

$$\chi^{(2)}_{\text{eff}}(\omega^a_1, \omega^c_3) = \chi^{(2)}_{\text{loc,R}} + \chi^{(2)}_{\text{loc,NR}} \cdot e^{i|\Delta k^{\text{SFG}}_z|z_2} \tag{14}$$

$$\chi^{(2)}_{\text{eff}}(\omega^a_1, -\omega^c_4) = \chi^{(2)}_{\text{loc,R}} + \chi^{(2)}_{\text{loc,NR}} \cdot e^{-i|\Delta k^{\text{DFG}}_z|z_2} \tag{15}$$

The resonant susceptibility $\chi^{(2)}_{\text{loc,R}}$ is a complex quantity. Its imaginary part describes the absorptive line shape of the vibrationally resonant transitions, whereas the real part consists of the corresponding dispersive line shape. According to (i) this resonant signal should equally contribute to the effective (measured) susceptibilities of the SFG and DFG pathways. In contrast, the nonresonant contribution $\chi^{(2)}_{\text{loc,NR}}$ is entirely real, independent of frequency, and should therefore form a straight line (offset) in the spectra. eqs 14 and 15 show that this signal should appear with slight phase shifts in the SFG/DFG spectra, leading to some leakage of the offset into the imaginary parts of the effective susceptibilities. However, because of the small thickness of the monolayer these phase shifts are very small. $\chi^{(2)}_{\text{loc,NR}}$ should therefore almost exclusively appear in the real part of the measured spectra with equal amplitudes for the SFG and DFG pathways.

The result of the SFG/DFG measurement of this sample is depicted in Figure 3A in the lower panel. All measurements in this publication are taken under PPP polarization conditions, which means that all interacting fields are p-polarized with respect to the sample surface. The imaginary and real parts of the spectra show the expected resonant contribution of the SAM (absorptive and dispersive line shapes, respectively), which is dominated by the asymmetric C−H stretch vibration of the terminal CH$_3$ group located at 2967 cm^{-1}. Furthermore, we can also observe the presence of the nonresonant contribution that causes the offset in the real parts of the measured susceptibilities (indicated by the light blue dotted line). Comparing SFG and DFG spectra (red and blue lines, respectively) we see that they indeed almost perfectly overlap as predicted by our theoretical concept. This good match includes the resonant line shapes and amplitudes in the real and imaginary parts as well as the nonresonant contribution. These experimental results therefore confirm the accuracy of relation (i).

We now turn to the experimental verification of the second fundamental aspect of the theoretical concept (cornerstone

(ii)) and, hence, the effect of depth contributions onto the measured SFG and DFG spectra. For this purpose, we perform SFG/DFG measurements with a second sample, a z-cut α quartz crystal. Alpha quartz shows a purely off-resonant nonlinear response,[50,51,75] and consequently its local susceptibility is real and forms a flat spectrum. However, because of its non-centrosymmetric crystal structure, nonlinear signals are generated in the entire bulk, which means that the majority of the nonlinear response originates from regions well-below the surface. If assumption (ii) is accurate, the measurement of this sample should yield clearly different SFG and DFG spectra, and we should observe depth-induced phase shifts with opposite sign in the two pathways.

On the basis of symmetry arguments[75] the overall nonlinear response of the sample can be divided into two distinct signal contributions, namely, one localized response that originates from the crystal surface ($\chi^{(2)}_{\text{loc,NR,I}}$, Figure 3B) and a second contribution, which corresponds to the bulk response ($\chi^{(2)}_{\text{loc,NR,B}}$, Figure 3B). The surface response is equivalent to the nonresonant response of the fused silica substrate; however, in this case it is located at $z_1 = 0$. To obtain the mathematical description of the bulk response the signal contributions from the bulk must be integrated in z, which can be done by setting $z' \rightarrow \infty$ in eqs 6 and 7. The resulting effective susceptibilities for the SFG and DFG pathways then read as follows.

$$\chi^{(2)}_{\text{eff}}(\omega^a_1, \omega^c_3) = \chi^{(2)}_{\text{loc,NR,I}} + \frac{\chi^{(2)}_{\text{loc,NR,B}}}{|\Delta k^{\text{SFG}}_z|} \cdot e^{i(\frac{\pi}{2})}$$

$$= \chi^{(2)}_{\text{loc,NR,I}} + i\frac{\chi^{(2)}_{\text{loc,NR,B}}}{|\Delta k^{\text{SFG}}_z|} \tag{16}$$

$$\chi^{(2)}_{\text{eff}}(\omega^a_1, -\omega^c_4) = \chi^{(2)}_{\text{loc,NR,I}} + \frac{\chi^{(2)}_{\text{loc,NR,B}}}{|\Delta k^{\text{DFG}}_z|} \cdot e^{-i(\frac{\pi}{2})}$$

$$= \chi^{(2)}_{\text{loc,NR,I}} - i\frac{\chi^{(2)}_{\text{loc,NR,B}}}{|\Delta k^{\text{DFG}}_z|} \tag{17}$$

We see that our mathematical framework indeed predicts deviations in the SFG and DFG spectra induced by the extended contribution from the depth. The integration of the bulk contribution in z causes the bulk response to appear phase-shifted by 90° (SFG) and −90° (DFG) in the effective susceptibilities, and consequently we should find the entire bulk signal in the imaginary parts of the measured spectra but with opposite signs. Moreover, the amplitudes of the bulk response should scale with the inverse of the corresponding wavevector mismatches. The calculation of the respective values for $|\Delta k_z|$ yields an expected amplitude ratio between the bulk contributions in the SFG and DFG spectra of 1/1.5 (see the Supporting Information). The surface contribution, however, can be expected to be much weaker and should appear in the real parts with equal sign and amplitude.

The results of the corresponding SFG/DFG measurement are shown in the lower panel of Figure 3B. In full agreement with our prediction, we see that nearly the entire nonlinear signal appears in the imaginary parts of the effective susceptibilities with the expected sign flip between the SFG and DFG spectra. Also, the amplitude ratio between the SFG and DFG responses precisely matches the predicted value of 1/1.5. Solely the comparatively small signature of the surface

contribution $\chi^{(2)}_{loc,NR,I}$ in the real parts of the spectra cannot be observed in this measurement (the real parts are essentially zero), although it definitely contributes to the overall response, as we will show later. Nevertheless, the main outcome of this comparison between theory and measurement is that the measured properties of the bulk signal precisely follow the theoretical prediction. Consequently, we can conclude that also the second cornerstone (ii) of our concept is experimentally validated.

■ DISCUSSION

So far, we have shown with the two experiments above that the key aspects of our presented mathematical framework are correct. We can now use the measurement of the z-cut quartz crystal to demonstrate how we can deduce important information about the spatial origin of the nonlinear signal from such SFG/DFG experiments. The observation that the SFG and DFG spectra deviate in phase directly shows that the measured signal cannot (exclusively) originate from the interface but that it must contain contributions that are generated below the surface. Furthermore, from the different absolute values of the amplitudes in the SFG and DFG spectra we learn that the signal source is not a localized response from some specific depth but rather a spatially expanded, integrated response (dependency of the amplitude on Δk_z). Finally, if we determine the phase difference between the SFG and DFG responses to extract the depth parameter z' we obtain ~180°, which corresponds to the value of $z' = \infty$. This shows that the response originates from the entire bulk of the crystal.

We see that, even in this quite trivial example of the quartz crystal, we may obtain a very rich and precise physical picture of the nonlinear sample properties using the SFG/DFG method. However, to establish the proposed concept for use in real experimental studies of samples with unknown depth profiles we need to verify how reliably and accurately we can determine *specific z-values* in a sample. This analysis of the depth accuracy of the presented method will be performed in two steps. We first discuss some general aspects of the depth resolution in such experiments and identify different effects that can have an impact on the accuracy of the obtained depth values. This discussion is very essential because it demonstrates the opportunities but also the limitations of the proposed SFG/DFG method. In a second step we analyze the accuracy of the method experimentally with a set of measurements on selected model samples.

Accuracy of the SFG/DFG Method. If we want to evaluate the depth precision of the proposed SFG/DFG method, we need to distinguish several sources of inaccuracies in the experimentally obtained values. The first potential uncertainty is the exact location of our reference plane ($z = 0$). The obtained z-values in all our experiments are relative quantities that signify the distances between the origin of a nonlinear signal and a reference plane. By its conception this reference plane is in our technique defined by the plane of linear reflection of the local oscillators. Its location and thus the position $z = 0$ is obviously dictated by the evolution of the refractive index in z across the interface. In many cases (e.g., at the interface between a flat solid substrate and air) this plane approximately coincides with the phase boundary,[76] a position that we would also have intuitively chosen to describe such an interfacial system. However, it is not difficult to imagine situations where this is not accurate. Examples are multilayered systems, rough surfaces, or systems where the phase boundary

is spatially "smeared out" to some extent (e.g., in liquids). In all these cases we will obtain an effective reference plane with a position that might deviate from the location of the very top phase boundary. An accurate interpretation of the obtained data must then account for such effects.

Another uncertainty about the $z = 0$ position can originate from experimental errors. As mentioned earlier, a phase-sensitive SFG/DFG experiment always consists of two measurements, namely, the measurement of the sample of interest and the measurement of an adequate reference sample with known nonlinear properties. Any phase errors in this referencing step will lead to phase errors in the obtained SFG and DFG spectra, which can ultimately result in erroneous shifts in the $z = 0$ position. The achievable accuracy of the reference phases for the SFG and DFG responses depends on many experimental factors and can vary for different experimental settings. As shown in the next section, typical values for the phase inaccuracies are on the order of ±3°, which corresponds to an uncertainty of the zero position of ca. ±1.3 nm. Note, however, that both effects described above only lead to uncertainties in the absolute location of $z = 0$ but not on the relative distance Δz between the origins of two different nonlinear signals. However, this is also limited as shown in the following.

Besides the general limitation of the achievable phase accuracy by the signal-to-noise ratio in the sample spectra there is another important effect that appears when multiple signal contributions from different depths are present. In the theoretical concept described in section III we considered only one single signal contribution, which originates from a specific depth (or depth profile), and we have shown that the determination of the signal origin in z can in these cases be done by simply extracting the phase difference between the obtained SFG and DFG spectra. If multiple signal contributions are simultaneously present, as it will be the case in most sample systems of interest, the respective complex susceptibilities $\chi^{(2)}_n$ simply add in the measured effective susceptibility. However, this does not apply to the corresponding phases ϕ_n (see eqs 18 and 19).

$$|\chi^{(2)}_{eff}| \cdot e^{i(\phi_{eff})} = \sum_n |\chi^{(2)}_n| \cdot e^{i(\phi_n)} \tag{18}$$

$$\phi_{eff} = a\,\tan 2\left(\sum_n |\chi^{(2)}_n| \cdot \sin(\phi_n), \sum_n |\chi^{(2)}_n| \cdot \cos(\phi_n)\right) \tag{19}$$

The obtained overall phase difference between the SFG and the DFG pathway is then a nontrivial function of the phases and amplitudes of all individual contributions. This property can make the accurate determination of the depth parameter z of a particular signal quite challenging and typically requires a precise decomposition of the overall spectra. The quality of this signal decomposition is therefore an important parameter that highly impacts the depth accuracy of the presented method.

The simplest way to isolate a particular signal is based on its spectrum. If the different signal contributions (e.g., resonance peaks) are spectrally well-separated such that each signal clearly dominates a particular spectral region the depth analysis is relatively straightforward. One can then determine the different depth parameters in good approximation by extracting the obtained phase differences in the respective frequency ranges. However, in cases where signals that
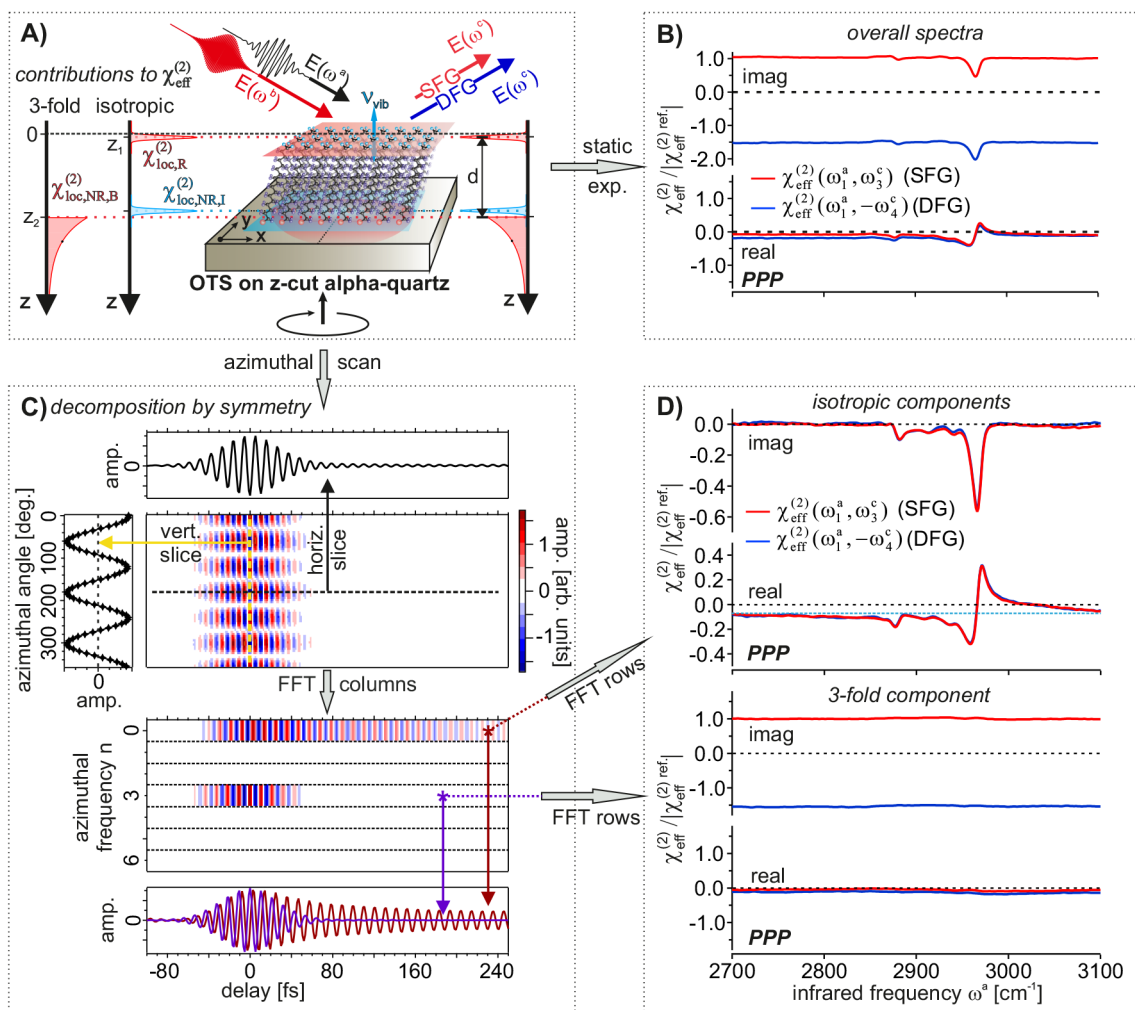
Figure 4. (A) Sketch showing the different signal contributions for the quartz-SAM sample; (B) static SFG/DFG measurement of the sample. The alpha-quartz crystal is oriented such that the bulk response is maximized; (C) decomposition of the contributions by symmetry (the corresponding DFG data are not shown). (upper panel) Time domain raw data of SFG/DFG measurements as a function of the azimuthal angle with vertical and horizontal slices through the 2D data matrix. (lower panel) Separation of the components with different azimuthal frequency by Fourier transformation along the vertical axis. For better visibility the threefold component is divided by the factor 6 to approximately match the amplitude of the isotropic component. (D) Decomposed SFG/DFG spectra obtained by Fourier transformation along the horizontal axis.

originate from different depths spectrally overlap, the situation becomes more difficult, and the application of an alternative and reliable way is required to either correctly decompose such spectra or to accurately determine the depth parameter of a specific signal in the presence of other contributions. As we will show in the next section, there are suitable analysis tools for both approaches that can be applied under certain circumstances.

Experimental Investigation of the Accuracy. With the discussion above we have shown that the achievable depth precision of the SFG/DFG method will highly depend on the experimental details of a particular measurement. In parallel, we saw that it depends on certain properties of the sample itself. Nevertheless, in this section we will demonstrate how far we can push the depth accuracy under realistic but beneficial experimental conditions.

For this purpose, we use a third sample type, where we functionalize a z-cut α quartz crystal with an OTS-SAM (see Figure 4A). The expected SFG/DFG response of this quartz-OTS sample is given by the following equations.

$$\chi_{\text{eff}}^{(2)}(\omega_1^a, \omega_3^c) = \chi_{\text{loc,R}}^{(2)} + \chi_{\text{loc,NR,I}}^{(2)} \cdot e^{i|\Delta k_z^{\text{SFG}}|z_2}$$

$$+ \frac{\chi_{\text{loc,NR,B}}^{(2)}}{|\Delta k_z^{\text{SFG}}|} \cdot e^{i(\frac{\pi}{2} + |\Delta k_z^{\text{SFG}}|z_2)} \tag{20}$$

$$\chi_{\text{eff}}^{(2)}(\omega_1^a, -\omega_4^c) = \chi_{\text{loc,R}}^{(2)} + \chi_{\text{loc,NR,I}}^{(2)} \cdot e^{-i|\Delta k_z^{\text{DFG}}|z_2}$$

$$+ \frac{\chi_{\text{loc,NR,B}}^{(2)}}{|\Delta k_z^{\text{DFG}}|} \cdot e^{-i(\frac{\pi}{2} + |\Delta k_z^{\text{DFG}}|z_2)} \tag{21}$$

We see that the overall nonlinear responses now consist of three contributions, namely, the resonant contribution of the molecular monolayer $\chi_{\text{loc,R}}^{(2)}$, the nonresonant response from the OTS-quartz interface $\chi_{\text{loc,NR,I}}^{(2)}$, and the bulk response of the quartz crystal $\chi_{\text{loc,NR,B}}^{(2)}$. In a first step we measure the static SFG/DFG spectra. The result of the measurement is shown in Figure 4B. As expected, we can clearly observe the presence of the two dominating contributions—the resonant spectroscopic signatures of the molecular monolayer and the bulk response

of the quartz crystal. These two signals have a comparable amplitude but originate from different depths within the sample. The origin of the resonant signal is spatially well-defined (z_1), while the bulk response of the quartz stems from the entire crystal. Because of this nonlocal nature, it is not possible to define a clear spatial origin for the bulk signal, but instead we have a well-defined depth for its onset (z_2). We can now use these two specific z coordinates in our accuracy study. The theoretically expected values for these two z coordinates can be calculated and compared to the results of the measurements. This allows one to evaluate the accuracy of the SFG/DFG method on two levels. By analyzing the phases of the resonant contribution, we can determine the experimental error in the $z = 0$ position and thus the accuracy of absolute z-values obtained in such experiments. Furthermore, the comparison of the measured distance between these coordinates with the theoretical value allows one to analyze the relative depth accuracy.

To perform this analysis, we need to precisely determine the phase differences between the SFG and the DFG responses for the resonant contribution and the nonresonant bulk contribution independently. On the basis of the spectra shown in Figure 4B this is highly nontrivial because of the large spectral overlap of the three contributions to the signals (in particular, the overlap between the two nonresonant contributions). In that respect the presented sample exactly corresponds to the challenging cases mentioned in the last section. To obtain the desired accuracy we clearly need to decompose the overall spectra.

Decomposition of the Spectra. A powerful way to separate different signal contributions in second-order non-linear spectroscopy is to perform an experimental symmetry analysis. If the susceptibility tensors that give rise to the different signals belong to different symmetry groups, they can often be separated by performing rotational anisotropy measurements.[41,75,77,78] A prominent example is the z-cut alpha-quartz crystal. While the surface contribution $\chi_{\mathrm{loc,NR,I}}^{(2)}$ shows an isotropic response the bulk contribution $\chi_{\mathrm{loc,NR,B}}^{(2)}$ oscillates with a period of 120° (threefold symmetry) upon azimuthal rotation of the crystal.[75] In the presented case there is additionally the signal contribution from the SAM. The molecular chains in an SAM typically show a slight tilt with respect to the surface normal,[79] which could lead to a component with onefold rotational symmetry in the resonant response. However, because of the relatively large focal spot in our experiment (ca. 0.13 mm^2) and the resulting averaging over many SAM domains with random tilt directions, it is safe to assume that the effective overall symmetry of the resonant response is isotropic.

As a consequence of the sample properties discussed above, it should be possible to separate the overall spectra by performing such a rotational anisotropy experiment into two parts: An isotropic part that contains the superposition of the resonant signal with the nonresonant surface contribution and a part with threefold symmetry containing the fully isolated bulk response of the quartz substrate. The corresponding experiment is done by performing consecutive phase-sensitive SFG/DFG measurements where we rotate the OTS-quartz sample in 5° increments about its surface normal. The resulting two-dimensional raw data set for the SFG response is shown in Figure 4C in the upper panel. Note, for better illustration we show in Figure 4C only the data of the SFG responses. The simultaneously obtained DFG data look very similar. The

presence of the quartz bulk contribution with its threefold azimuthal symmetry can clearly be observed in the raw data (see for better clarity the vertical slice through the raw data at 0 fs time delay in the upper left panel of Figure 4C).

The threefold and isotropic contributions can now be separated by Fourier transformation of the 2D raw data matrix in the vertical direction. The resulting two-dimensional SFG data set is depicted in Figure 4C in the lower panel. Here we indeed find responses in the two expected symmetry classes (isotropic $n = 0$ and threefold $n = 3$). After this separation we retrieve the corresponding SFG/DFG spectra by Fourier transformation of the two separated parts along the horizontal axis (see Figure 4D). The equations that describe the contributions to the isotropic SFG and DFG spectra are given by

$$\chi_{\mathrm{eff},n=0}^{(2)}(\omega_1^{\mathrm{a}}, \omega_3^{\mathrm{c}}) = \chi_{\mathrm{loc,R}}^{(2)} + \chi_{\mathrm{loc,NR,I}}^{(2)} \cdot e^{i|\Delta k_z^{\mathrm{SFG}}|z_2} \tag{22}$$

$$\chi_{\mathrm{eff},n=0}^{(2)}(\omega_1^{\mathrm{a}}, -\omega_4^{\mathrm{c}}) = \chi_{\mathrm{loc,R}}^{(2)} + \chi_{\mathrm{loc,NR,I}}^{(2)} \cdot e^{-i|\Delta k_z^{\mathrm{DFG}}|z_2} \tag{23}$$

and the expressions for the threefold component are accordingly

$$\chi_{\mathrm{eff},n=3}^{(2)}(\omega_1^{\mathrm{a}}, \omega_3^{\mathrm{c}}) = \frac{\chi_{\mathrm{loc,NR,B}}^{(2)}}{|\Delta k_z^{\mathrm{SFG}}|} \cdot e^{i(\frac{\pi}{2} + |\Delta k_z^{\mathrm{SFG}}|z_2)} \tag{24}$$

$$\chi_{\mathrm{eff},n=3}^{(2)}(\omega_1^{\mathrm{a}}, -\omega_4^{\mathrm{c}}) = \frac{\chi_{\mathrm{loc,NR,B}}^{(2)}}{|\Delta k_z^{\mathrm{DFG}}|} \cdot e^{-i(\frac{\pi}{2} + |\Delta k_z^{\mathrm{DFG}}|z_2)} \tag{25}$$

Comparing expressions 22 and 23 to eqs 14 and 15 shows that the SFG and DFG spectra of the isotropic component should resemble very closely the spectra that we obtained from the FS-SAM sample in Figure 3A. A closer look into these spectra reveals that this is indeed the case. The spectra from Figure 4D upper panel and 3A look essentially the same (including the negative offset in the real parts due to the contribution of the nonresonant surface signal). The SFG and DFG spectra of the threefold component should in contrast not contain any spectroscopic signatures of the vibrational resonances. As shown in Figure 4D in the lower panel, also this prediction is precisely fulfilled.

Absolute Depth Accuracy. At this point we have successfully decomposed the overall responses into two parts separating the two signal sources that we want to use for the intended analysis. We can now proceed with the determination of the two z-coordinates from the obtained spectra. We start with the analysis of the isotropic part and the evaluation of the experimental uncertainty in the $z = 0$ position.

As mentioned earlier the reference plane ($z = 0$) should be located precisely at the very top interface (SAM/air), which should coincide with the spatial origin of the resonant signal. We can now mathematically describe possible deviations from this position (e.g., induced by improper phasing) by introducing an error phase σ in the equations. All SFG and DFG responses are therefore multiplied by the factors $e^{i\frac{\sigma}{2}}$ and $e^{-i\frac{\sigma}{2}}$, respectively. The expressions for the isotropic part then transform to

$$\chi_{\mathrm{eff},n=0}^{(2)}(\omega_1^{\mathrm{a}}, \omega_3^{\mathrm{c}}) = \chi_{\mathrm{loc,R}}^{(2)} \cdot e^{i\frac{\sigma}{2}} + \chi_{\mathrm{loc,NR,I}}^{(2)} \cdot e^{i(|\Delta k_z^{\mathrm{SFG}}|z_2 + \frac{\sigma}{2})} \tag{26}$$

and

$$\chi_{\text{eff},n=0}^{(2)}(\omega_1^a, -\omega_4^c) = \chi_{\text{loc,R}}^{(2)} \cdot e^{-i\frac{\sigma}{2}} + \chi_{\text{loc,NR,I}}^{(2)} \cdot e^{-i(|\Delta k_z^{\text{DFG}}|z_2 + \frac{\sigma}{2})}$$

(27)

If we determine the exact value for σ in a given experiment, we can quantify these phasing errors and transform them into a position error for the resonant response. In order to obtain σ from the isotropic part of the measured spectra we exploit the different spectral line shapes of the two signal contributions $\chi_{\text{loc,R}}^{(2)}$ and $\chi_{\text{loc,NR,I}}^{(2)}$. If we form the difference between the complex SFG and DFG spectra we get following expression.

$$\Delta\chi_{\text{eff},n=0}^{(2)} = 2i \cdot \left(\chi_{\text{loc,R}}^{(2)} \cdot \sin\left(\frac{\sigma}{2}\right) \right.$$
$$\left. + \chi_{\text{loc,NR,I}}^{(2)} \cdot \sin\left(\frac{\sigma + (|\Delta k_z^{\text{SFG}}| + |\Delta k_z^{\text{DFG}}|)z_2}{2}\right) \right)$$

(28)

We see that, in the case of $\sigma = 0$, the resonance signal should vanish in the difference spectrum, and the only remaining spectral feature would be a straight line originating from some residual of the nonresonant surface signal. Any deviations from $\sigma = 0$ will, in turn, make the spectroscopic signatures of the resonance become apparent. On the basis of this property we can determine σ with great precision. We therefore generate from the obtained isotropic spectra a series of difference spectra, where we introduce an artificial phase spread ϵ between the SFG and DFG responses. Subsequently we evaluate the deviation $P(\epsilon)$ of these difference spectra from a straight line. The phase value where $P(\epsilon)$ reaches its minimum then corresponds to $-\sigma$. In practice this is done in an automated procedure that minimizes the following function

$$P(\epsilon) =$$
$$\int d\omega_1 |\chi_{\text{eff},n=0}^{(2)}(\omega_1^a, \omega_3^c) \cdot e^{i\frac{\epsilon}{2}}$$
$$- \chi_{\text{eff},n=0}^{(2)}(\omega_1^a, -\omega_4^c) \cdot e^{-i\frac{\epsilon}{2}} - C_\epsilon(\omega_1)|^2$$

(29)

where $C_\epsilon(\omega_1)$ represents the residual nonresonant contribution that is obtained by a linear fit of each individual difference spectra. The results of this procedure for the quartz-OTS sample are depicted in Figure 5.

The evolution of the difference spectra (their modulus square) with ϵ clearly shows how the spectroscopic signatures of the resonances disappear at the minimum of the deviation
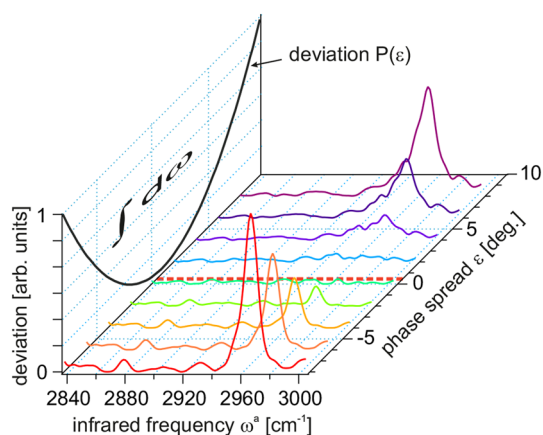

Figure 5. Spectral deviation as a function of phase spread ϵ. Red dotted line marks the minimum of the deviation curve.

curve. This minimum is, in this particular example, located at ϵ = 0.1°, corresponding to an error phase of $\sigma = -0.1°$. This nonzero error phase leads to a shift of the reference plane and ultimately to a shift of the apparent z position of the resonant signal $(z_1(\sigma))$ from zero. The latter can be obtained using following relation.

$$\sigma = (|\Delta k_z^{\text{SFG}}| + |\Delta k_z^{\text{DFG}}|)z_1(\sigma)$$

(30)

Assuming a refractive index inside the SAM of 1.46,[72] the calculation of the sum of the wavevector mismatches yields for our experimental geometry a value of 2.3°/nm (see the Supporting Information). Using this value in eq 30, we obtain an apparent position of $z_1(\sigma) = -0.04$ nm. Compared to the expected value of zero this is a very close match. On the basis of the analysis of the results from experiments with similar samples we find that the obtained values for ϵ show typical deviations on the order of $\pm 3°$. From this we can deduce that the uncertainty of the $z = 0$ position is on the order of ± 1.3 nm (for the experimental settings used in the presented studies).

Relative Depth Accuracy. We now turn our attention to the analysis of the relative depth accuracy of the method. For this we need to determine the distance d between the measured z-coordinates of the resonant response and the onset of the quartz bulk contribution. Note, both signals are acquired within the same measurement, which means that both are impacted by phasing errors in the same way. The distance is therefore simply given by

$$d = z_2 - z_1(\sigma)$$

(31)

Since the bulk response is fully isolated in the threefold part $\chi_{\text{eff},n=3}^{(2)}$, we can determine z_2 directly by analyzing the phase difference $\Delta\phi(\chi_{\text{eff},n=3}^{(2)})$ between the SFG and DFG spectra. Using eqs 24 and 25 we find the following relation.

$$z_2 = \frac{\Delta\phi(\chi_{\text{eff},n=3}^{(2)}) - \pi}{|\Delta k_z^{\text{SFG}}| + |\Delta k_z^{\text{DFG}}|}$$

(32)

Applying eqs 31 and 32 to our measured data we can extract d from the experimental results. Since the phases of the nonlinear responses are spectrally resolved in the presented measurements, we also obtain the values for d as a function of vibrational frequency. We note that the location of the onset of the bulk response is obviously independent of the frequency. The resulting spectrum should therefore form a straight line with a constant offset from zero.

The result of this analysis is shown in Figure 6B (red line). We indeed observe for d a straight line that is offset from zero. The mean value of d amounts to ~4.2 nm. The positive sign of this z-coordinate thereby indicates that the onset of the bulk signal lies as expected below the SAM/air interface. In order to evaluate the accuracy of this experimentally obtained value we need to theoretically estimate the distance d. In a simple picture we would expect that d precisely equals the chain length of the aliphatic carbon chain in the SAM in its straightened form (see Figure 6 middle panel). The OTS molecule that forms the SAM in the presented measurements contains 18 carbon units and has a chain length of ~2.4 nm. Although our measured value lies indeed in the same ballpark, the two values do considerably deviate. In total the measured value is 1.8 nm larger than the estimated thickness of the molecular monolayer. This discrepancy could be interpreted as inaccuracy in the measurement, but several repetitions of the experiment yield the very same reported value.
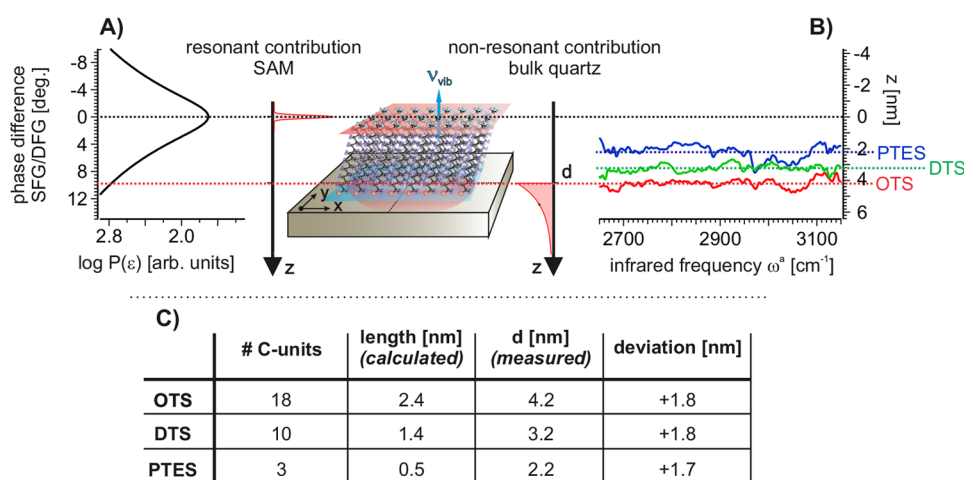
Figure 6. Determination of the distance d between the resonant signal and the onset of the quartz bulk response. (A) Spectral deviation as a function of phase spread ϵ (from Figure 5) for the determination of the spatial origin of the resonance signal; (B) spatial origin for the onset of the quartz bulk signal. The curves in (A, B) are shifted in z such that the origin of the resonant signals is at $z_1 = 0$, and the mean values in (B) therefore correspond to d; (C) comparison between calculated and measured values for the different SAMs.

To further investigate this observation, we performed similar experiments with different thicknesses of the molecular SAMs. Z-cut quartz crystals are therefore functionalized with decyltrichlorosilane (DTS, 10 carbon units) and propyltriethoxysilane (PTES, 3 carbon units) with calculated chain lengths of ca. 1.4 and 0.5 nm, respectively. After performing the same data analysis as shown for the OTS case, we obtain the resulting curves depicted Figure 6B (green DTS, blue PTES). Comparing the three curves corresponding to the three different SAMs, we can clearly see that they are indeed shifted in z with respect to each other. All measured values and calculated chain lengths are summarized in the table in Figure 6C. A closer look onto these data shows that our measured values precisely follow the trend of the calculated chain lengths for the three different SAMs. The individual differences in chain length of ~1 nm are perfectly reproduced by the measured data. These results clearly show that we can resolve depth differences as small as 1 nm using the SFG/DFG technique, which suggests that the relative depth accuracy readily reaches into the sub-nanometer region.

The only discrepancy between the experimental and theoretical values is the presence of the constant offset of ~1.8 nm in the measured data. The reproducibility of this deviation and the high accuracy of the obtained relative depth values strongly point into the direction that this offset relates to a property of the samples rather than to the spectroscopic technique itself. This suggests that we should go one step back in our interpretation of the obtained data and refine our physical picture of the samples measured in this section.

The distance d that we measure is the distance between the top of the SAM and the onset of the bulk signal. This value equals the molecular chain length only if the z-coordinate for the onset of the bulk contribution is precisely located at the quartz−SAM interface. However, this is not necessarily the case. For the generation of a second-order bulk signal the crystal structure needs to be non-centrosymmetric. Although this is certainly given inside the bulk of α quartz, it is not clear to what extent this well-defined crystal structure continues in an unperturbed manner up to the crystal surface. Several studies have shown that the surface of α quartz can be considerably reconstructed and that the nature of these surface

modifications highly depends on the thermal history of the crystal.[80,81] How deep into the bulk these structural modifications reach is currently unknown. But if we consider that the surfaces of our quartz crystals are optically polished, which involves applying a mechanical stress to the surface and generating elevated local temperatures, it is not unreasonable to assume that there are significant structural distortions at the crystal surface that extend over relevant length scales into the subsurface region. These structural distortions form a defect-rich spacer layer that spatially separates the bulk crystal from the molecular monolayer. The presence of such a layer would manifest itself spectroscopically by an effective depth for the onset of the bulk signal that lies somewhat below the surface of the crystal, just like the shift that we observe in our data. In fact, such effects in the nonlinear response of the z-cut quartz crystal have also been observed and discussed in a recent publication by Sun and co-workers.[50] We therefore assign the observed 1.8 nm shift in the measured data to the effect of these structural distortions. In consequence, our data suggest that the effective onset of the bulk signal in our quartz samples is located 1.8 nm below the quartz−SAM interface, a value that definitely seems realistic. However, besides this rationalizing argumentation we found further experimental evidence in support of the presented interpretation during our studies on these samples.

Following the discussion above one would expect that the amount of structural distortions (and thus the value for the offset) sensitively depends on the details of the polishing process. In the article in ref 50 the authors show evidence for just such a dependency. For this reason, we used in the experiments shown in this section only quartz crystals of the same type and from the same vendor to ensure a maximum of similarity in the polishing. As a result, we obtained the reported constant offset. In test measurements with quartz crystals from a different vendor and thus potentially different polishing, however, we did observe significant deviations in the value for the offset. This dependence on the sample history clearly suggests that the observed shift is indeed related to the intrinsic properties of the quartz crystal, which is in full accordance with the presented interpretation. With this explanation for the observed offset in hand all the measured

values become entirely conclusive, and we can therefore consider the reported relative accuracy to be confirmed.

Conclusions. In conclusion of this experimental investigation presented above we can state that the SFG/DFG technique shows a remarkable precision. The measurements reveal that the relative depth accuracy can even reach the sub-nanometer regime, while the accuracy of the obtained absolute z-coordinates is slightly lower with typical position errors on the order of ± 1.3 nm.

We have also seen that one of the main challenges for the depth analysis of such measurements is the isolation of a particular signal of interest from the overall spectra. In the presented example the separation of the signals required an admittedly quite extensive effort on the experimental side (e.g., the rotational anisotropy measurements) and in the data analysis. We would like to point out that, for many sample systems of interest, such additional measurements are not necessarily required. The reason for the choice of the quartz−SAM samples as a model system despite this increased complexity is mainly based on their well-defined structures and well-understood nonlinear properties, which makes them suitable for the evaluation of the depth accuracy. But there is also a direct benefit from the use of a spectroscopically rather challenging model system in the presented study: it gave us the opportunity to discuss and present first examples of advanced techniques for the decomposition of different signal contributions and in the data analysis, which are certainly key ingredients of the SFG/DFG method.

Furthermore, the study also allows us to directly evaluate their performance. From the high-precision results that we obtained in the end of this study we can conclude that the application of these techniques did not noticeably degrade the accuracy of the data. On the contrary, at each step during the detailed analysis of the nonlinear responses from the investigated samples we repeatedly compared the obtained experimental data with the corresponding theoretical predictions, and without exception we have found almost perfect agreement. This shows that our presented mathematical framework builds a solid foundation for describing the measured SFG and DFG data, which is an important basis to further develop and refine our data analysis techniques.

Finally, we briefly discuss the information content that we obtain with the presented technique. The result part of this publication focuses on the evaluation of the depth accuracy of the method, and as test parameter we use the layer thickness of our quartz−SAM samples. This layer thickness could have been also determined with alternative, more traditional spectroscopic techniques such as ellipsometry,[82,83] which can yield a similar depth resolution. While it is beyond the scope of this publication to compare the performance of our nonlinear technique with ellipsometry, it is important to note that the information content of the data obtained here is fundamentally different: in the presented study we have not only precisely determined the spatial origin of different signal sources but also have obtained, in particular, the corresponding nonlinear vibrational spectra for each of these signal contributions (see, e.g., the vibrationally resonant spectra of the SAM). It is this duality of information that allows us to analyze the chemical composition and structures in the sample and directly correlate them to specific spatial coordinates. Furthermore, our technique is sensitive to spatial changes in symmetry rather than changes in the refractive index (as is the case for linear interferometric techniques). A good example illustrating this

difference is in fact contained in the presented results. In the accuracy study we found that the onset of the nonlinear bulk signal is not located at the quartz−SAM interface (where the refractive index changes) but 1.8 nm below, where the symmetry of the crystal adopts the bulk properties. This sensitivity to symmetry changes is, however, one of the fundamental requirements for the intended investigations of the properties of extended interfacial regions as described in the Introduction.

Overall, the presented SFG/DFG method combines vibrational, spatial, and symmetry information in a unique fashion, and it is this combination that gives exciting new perspectives for interfacial studies and sets this technique apart from more traditional spectroscopies.

■ SUMMARY AND OUTLOOK

In this contribution we have presented a technique that allows one to obtain deep insight into the physics of extended interfacial regions by combining phase-sensitive SFG and DFG spectroscopy. The method has been described theoretically, and the feasibility and high accuracy of such measurements have been demonstrated experimentally. This sets the basis for moving toward the spectroscopic characterization of more challenging and scientifically relevant interfaces, like the air/liquid and solid/liquid interfaces, and for tackling longstanding questions concerning the actual interfacial volume that participates in what is generally described as "interfacial signal".

However, the most important implication of our work is more fundamental, as it describes the way to determine important spectroscopic observables in nonlinear spectroscopic experiments by selectively measuring the signals from different nonlinear interaction pathways. This concept is very general and can also be applied to tackle other physical problems beyond the analysis of depth profiles. An example is the precise determination of nonlinear Fresnel factors, a technique that could have an important impact in the evolving field of spectro-electrochemistry (this will be the topic in a separate publication). Furthermore, the basic principle of the method described here is not restricted to second-order processes and could straightforwardly be adopted by other spectroscopic methods within the diverse family of coherent nonlinear techniques. A very promising candidate that naturally comes to mind is the third-order coherent anti-Stokes Raman spectroscopy (CARS).[84] Overall, the presented work provides a promising perspective for the evolving field of nonlinear spectroscopy toward a higher level of accessible information and reduced necessity for theoretical models to extract the desired physical quantities from the obtained spectra.

■ ASSOCIATED CONTENT

ⓢ Supporting Information

The Supporting Information is available free of charge at https://pubs.acs.org/doi/10.1021/acs.jpcc.2c01324.

> Details on symmetry properties of the local susceptibility and calculation of wavevectors

■ AUTHOR INFORMATION

Corresponding Author

Martin Thämer − *Department of Physical Chemistry, Fritz-Haber-Institut of the Max Planck Society, 14195 Berlin, Germany;* ⓞ orcid.org/0000-0002-9631-9280; Email: thaemer@fhi-berlin.mpg.de

Authors

Vasileios Balos − *Department of Physical Chemistry, Fritz-Haber-Institut of the Max Planck Society, 14195 Berlin, Germany; IMDEA Nanoscience, 28049 Madrid, Spain;* ⊙ orcid.org/0000-0001-7606-6653

Tobias Garling − *Department of Physical Chemistry, Fritz-Haber-Institut of the Max Planck Society, 14195 Berlin, Germany*

Alvaro Diaz Duque − *Department of Physical Chemistry, Fritz-Haber-Institut of the Max Planck Society, 14195 Berlin, Germany*

Ben John − *Department of Physical Chemistry, Fritz-Haber-Institut of the Max Planck Society, 14195 Berlin, Germany*

Martin Wolf − *Department of Physical Chemistry, Fritz-Haber-Institut of the Max Planck Society, 14195 Berlin, Germany*

Complete contact information is available at:
https://pubs.acs.org/10.1021/acs.jpcc.2c01324

■ REFERENCES

(1) Ohsima, H. *Biophysical Chemistry of Biointerfaces;* John Wiley and Sons, Inc., 2010.

(2) Barthelat, F.; Yin, Z.; Buehler, M. J. Structure and mechanics of interfaces in biological materials. *Nature Reviews Materials* **2016**, *1*, 1−16.

(3) Hosseinpour, S.; Roeters, S. J.; Bonn, M.; Peukert, W.; Woutersen, S.; Weidner, T. Structure and Dynamics of Interfacial Peptides and Proteins from Vibrational Sum-Frequency Generation Spectroscopy. *Chem. Rev.* **2020**, *120*, 3420−3465.

(4) Alamdari, S.; Roeters, S. J.; Golbek, T. W.; Schmüser, L.; Weidner, T.; Pfaendtner, J. Orientation and Conformation of Proteins at the Air-Water Interface Determined from Integrative Molecular Dynamics Simulations and Sum Frequency Generation Spectroscopy. *Langmuir* **2020**, *36*, 11855−11865.

(5) Zhang, J.-x.; Aiello, D.; Aker, P. M. A spectroscopic tour through the liquid aerosol interface: Implications for atmospheric chemictry. *Journal of Gorphysical Research* **1994**, *99*, 25667.

(6) Jungwirth, P.; Tobias, D. J. Molecular structure of salt solutions: A new view of the interface with implications for heterogeneous atmospheric chemistry. *J. Phys. Chem. B* **2001**, *105*, 10468−10472.

(7) Herrmann, H. Kinetics of Aqueous Phase Reactions Relevant for Atmospheric Chemistry. *Chem. Rev.* **2003**, *103*, 4691−4716.

(8) Li, Z.; Liu, Y.; Wang, D.; Wang, P.; Xu, R.; Xie, D. Characterizing surface electrochemical properties of simulated bulk soil in situ by streaming potential measurements. *European Journal of Soil Science* **2019**, *70*, 1063−1072.

(9) Wandelt, K. *Encyclopedia of Interfacial Chemistry;* Elsevier, 2018.

(10) Zwaschka, G.; Wolf, M.; Campen, R. K.; Tong, Y. A Microscopic Model of the Electrochemical Vibrational Stark Effect: Understanding VSF Spectroscopy of (bi)Sulfate on Pt(111). *Surf. Sci.* **2018**, *678*, 78−85.

(11) Sinfelt, J. H. Role of surface science in catalysis. *Surf. Sci.* **2002**, *500*, 923−946.

(12) Somorjai, G. A. The surface science of heterogeneous catalysis. *Surf. Sci.* **1994**, *299-300*, 849.

(13) Matijevic, E. *Surface and Colloid Science;* Plenum Press, 1982.

(14) Wickman, H. H.; Korley, J. N. Colloid crystal self-organization and dynamics at the air/water interface. *Nature* **1998**, *393*, 445−447.

(15) Pezzotti, S.; Galimberti, D. R.; Shen, Y. R.; Gaigeot, M. P. Structural definition of the BIL and DL: A new universal methodology to rationalize non-linear: $\chi(2)(\omega)$ SFG signals at charged interfaces, including $\chi(3)(\omega)$ contributions. *Phys. Chem. Chem. Phys.* **2018**, *20*, 5190−5199.

(16) Walker, D. S.; Richmond, G. L. Interfacial depth profiling of the orientation and bonding of water molecules across liquid-liquid interfaces. *J. Phys. Chem. C* **2008**, *112*, 201−209.

(17) Mezger, M.; Roth, R.; Schröder, H.; Reichert, P.; Pontoni, D.; Reichert, H. Solid-liquid interfaces of ionic liquid solutions - Interfacial layering and bulk correlations. *J. Chem. Phys.* **2015**, *142*, 164707.

(18) Glosli, J. N.; Philpott, M. R. Molecular dynamics study of interfacial electric fields. *Electrochim. Acta* **1996**, *41*, 2145−2158.

(19) Jungwirth, P.; Tobias, D. J. Specific ion effects at the air/water interface. *Chem. Rev.* **2006**, *106*, 1259−1281.

(20) Eftekhari-Bafrooei, A.; Borguet, E. Effect of surface charge on the vibrational dynamics of interfacial water. *J. Am. Chem. Soc.* **2009**, *131*, 12034−12035.

(21) Powell, C. J.; Jablonski, A. Progress in quantitative surface analysis by X-ray photoelectron spectroscopy: Current status and perspectives. *J. Electron Spectrosc. Relat. Phenom.* **2010**, *178−179*, 331−346.

(22) Nagy, Z.; You, H. Applications of surface X-ray scattering to electrochemistry problems. *Electrochim. Acta* **2002**, *47*, 3037−3055.

(23) Bianconi, A. Surface X-Ray Absorption Spectroscopy: Surface Exafs and Surface Xanes. *Applications of surface science* **1980**, *6*, 392−418.

(24) Henzler, M. LEED studies of surface imperfections. *Applications of Surface Science* **1982**, *11-12*, 450.

(25) Brown, M. A.; Faubel, M.; Winter, B. X-Ray photo- and resonant Auger-electron spectroscopy studies of liquid water and aqueous solutions. *Annual Reports on the Progress of Chemistry - Section C* **2009**, *105*, 174−212.

(26) Powell, C. J.; Jablonski, A. Surface Sensitivity of Auger-Electron Spectroscopy and X-ray Photoelectron Spectroscopy. *Journal of Surface Analysis* **2011**, *17*, 170−176.

(27) Du, Q.; Superfine, R.; Freysz, E.; Shen, Y. R. Vibrational spectroscopy of water at the vapor/water interface. *Phys. Rev. Lett.* **1993**, *70*, 2313.

(28) Eisenthal, K. B. Liquid interfaces probed by second-harmonic and sum-frequency spectroscopy. *Chem. Rev.* **1996**, *96*, 1343.

(29) Geiger, F. M. Second harmonic generation, sum frequency generation, and X(3): Dissecting environmental interfaces with a nonlinear optical swiss army knife. *Annu. Rev. Phys. Chem.* **2009**, *60*, 61−83.

(30) Pijolat, M.; Hollinger, G. New depth-profiling method by angular-dependent X-ray photoelectron spectroscopy. *Surf. Sci.* **1981**, *105*, 114−128.

(31) Cumpson, P. J. Angle-resolved XPS depth-profiling strategies. *Appl. Surf. Sci.* **1999**, *144−145*, 16−20.

(32) Neerinck, D. G.; Vink, T. J. Depth profiling of thin IT0 films by grazing incidence X-ray diffraction. *Thin Solid Films* **1996**, *278*, 12−17.

(33) Bedzyk, M. J.; Bilderback, D.; White, J.; Abruña, H. D.; Bommarito, M. G. Probing electrochemical interfaces with X-ray standing waves. *J. Phys. Chem.* **1986**, *90*, 4926−4928.

(34) Fadley, C. S. Hard X-ray photoemission with angular resolution and standing-wave excitation. *J. Electron Spectrosc. Relat. Phenom.* **2013**, *190*, 165−179.

(35) Nemšák, S.; Shavorskiy, A.; Karslioglu, O.; Zegkinoglou, I.; Rattanachata, A.; Conlon, C. S.; Keqi, A.; Greene, P. K.; Burks, E. C.; Salmassi, F.; et al. Concentration and chemical-state profiles at heterogeneous interfaces with sub-nm accuracy from standing-wave ambient-pressure photoemission. *Nat. Commun.* **2014**, *5*, 1−7.

(36) Gray, A. X. Future directions in standing-wave photoemission. *J. Electron Spectrosc. Relat. Phenom.* **2014**, *195*, 399−408.

(37) Guyot-Sionnest, P.; Hunt, J. H.; Shen, Y. R. Sum-frequency vibrational spectroscopy of a Langmuir film: Study of molecular orientation of a two-dimensional system. *Phys. Rev. Lett.* **1987**, *59*, 1597−1600.

(38) Zhu, X. D.; Suhr, H.; Shen, Y. R. Surface vibrational spectroscopy by infrared-visible sum frequency generation. *Phys. Rev. B* **1987**, *35*, 3047−3050.

(39) Shen, Y. R. Surface properties probed by second-harmonic and sum-frequency generation. *Nature* **1989**, *337*, 519.

(40) Le Rille, A.; Tadjeddine, A. In situ visible-infrared sum and difference frequency generation at the electrochemical interface. *J. Electroanal. Chem.* **1999**, *467*, 238−248.

(41) Boyd, R. W. *Nonlinear Optics,* 3rd ed.; Academic Press, 2007.

(42) Shen, Y. R. *Fundamentals of Sum Frequency Spectroscopy*; Cambridge University Press, 2016.

(43) Morita, A. *Theory of Sum Frequency Generation Spectroscopy*; Springer Nature Singapore, 2018.

(44) Yamaguchi, S. Development of single-channel heterodyne-detected sum frequency generation spectroscopy and its application to the water/vapor interface. *J. Chem. Phys.* **2015**, *143*, 034202.

(45) Wang, J.; Bisson, P. J.; Marmolejos, J. M.; Shultz, M. J. Measuring Complex Sum Frequency Spectra with a Nonlinear Interferometer. *J. Phys. Chem. Lett.* **2016**, *7*, 1945−1949.

(46) Stiopkin, I. V.; Jayathilake, H. D.; Bordenyuk, A. N.; Benderskii, A. V. Heterodyne-Detected Vibrational Sum Frequency Generation Spectroscopy. *J. Am. Chem. Soc.* **2008**, *130*, 2271−2275.

(47) Yamaguchi, S.; Tahara, T. Heterodyne-detected electronic sum frequency generation: "Up" versus "down" alignment of interfacial molecules. *J. Chem. Phys.* **2008**, *129*, 101102.

(48) Wang, H.; Gao, T.; Xiong, W. Self-Phase-Stabilized Heterodyne Vibrational Sum Frequency Generation Microscopy. *ACS Photonics* **2017**, *4*, 1839−1845.

(49) Schweizer, T.; Nicolau, B. G.; Cavassin, P.; Feurer, T.; Banerji, N.; Réhault, J. High-resolution phase-sensitive sum frequency generation spectroscopy by time-domain ptychography. *Opt. Lett.* **2020**, *45*, 6082−6085.

(50) Sun, S.; Liang, R.; Xu, X.; Zhu, H.; Shen, Y. R.; Tian, C. Phase reference in phase-sensitive sum-frequency vibrational spectroscopy. *J. Chem. Phys.* **2016**, *144*, 244711.

(51) Hu, X. H.; Wei, F.; Wang, H.; Wang, H. F. α-Quartz Crystal as Absolute Intensity and Phase Standard in Sum-Frequency Generation Vibrational Spectroscopy. *J. Phys. Chem. C* **2019**, *123*, 15071−15086.

(52) Pool, R. E.; Versluis, J.; Backus, E. H.; Bonn, M. Comparative study of direct and phase-specific vibrational sum-frequency generation spectroscopy: Advantages and limitations. *J. Phys. Chem. B* **2011**, *115*, 15362−15369.

(53) Shen, Y. R. Phase-sensitive sum-frequency spectroscopy. *Annu. Rev. Phys. Chem.* **2013**, *64*, 129−150.

(54) Chen, S. L.; Fu, L.; Gan, W.; Wang, H. F. Homogeneous and inhomogeneous broadenings and the Voigt line shapes in the phase-resolved and intensity sum-frequency generation vibrational spectroscopy. *J. Chem. Phys.* **2016**, *144*, 034704.

(55) Vanselous, H.; Petersen, P. B. Extending the Capabilities of Heterodyne-Detected Sum-Frequency Generation Spectroscopy: Probing Any Interface in Any Polarization Combination. *J. Phys. Chem. C* **2016**, *120*, 8175−8184.

(56) Sengupta, S.; Moberg, D. R.; Paesani, F.; Tyrode, E. Neat Water-Vapor Interface: Proton Continuum and the Nonresonant Background. *J. Phys. Chem. Lett.* **2018**, *9*, 6744−6749.

(57) Thämer, M.; Campen, R. K.; Wolf, M. Detecting weak signals from interfaces by high accuracy phase-resolved SFG spectroscopy. *Phys. Chem. Chem. Phys.* **2018**, *20*, 25875−25882.

(58) Gonella, G.; Lütgebaucks, C.; De Beer, A. G.; Roke, S. Second harmonic and sum-frequency generation from aqueous interfaces is modulated by interference. *J. Phys. Chem. C* **2016**, *120*, 9165−9173.

(59) Tong, Y.; Zhao, Y.; Li, N.; Osawa, M.; Davies, P. B.; Ye, S. Interference effects in the sum frequency generation spectra of thin organic films. I. Theoretical modeling and simulation. *J. Chem. Phys.* **2010**, *133*, 034704.

(60) Ohno, P. E.; Chang, H.; Spencer, A. P.; Liu, Y.; Boamah, M. D.; Wang, H. F.; Geiger, F. M. Beyond the Gouy-Chapman Model with Heterodyne-Detected Second Harmonic Generation. *J. Phys. Chem. Lett.* **2019**, *10*, 2328−2334.

(61) Laaser, J. E.; Xiong, W.; Zanni, M. T. Time-domain SFG spectroscopy using mid-IR pulse shaping: Practical and intrinsic advantages. *J. Phys. Chem. B* **2011**, *115*, 2536−2546.

(62) Ohno, P. E.; Saslow, S. A.; Wang, H. F.; Geiger, F. M.; Eisenthal, K. B. Phase-referenced nonlinear spectroscopy of the α-quartz/water interface. *Nat. Commun.* **2016**, *7*, 1−5.

(63) Dalstein, L.; Chiang, K. Y.; Wen, Y. C. Direct Quantification of Water Surface Charge by Phase-Sensitive Second Harmonic Spectroscopy. *J. Phys. Chem. Lett.* **2019**, *10*, 5200−5205.

(64) Garling, T.; Campen, R. K.; Wolf, M.; Thämer, M. A General Approach to Combine the Advantages of Collinear and Noncollinear Spectrometer Designs in Phase-Resolved Second-Order Nonlinear Spectroscopy. *J. Phys. Chem. A* **2019**, *123*, 11022−11030.

(65) Barrett, A.; Petersen, P. B. Order of Dry and Wet Mixed-Length Self-Assembled Monolayers. *J. Phys. Chem. C* **2015**, *119*, 23943−23950.

(66) Pikalov, A. A.; Ngo, D.; Lee, H. J.; Lee, T. R.; Baldelli, S. Sum Frequency Generation Imaging Microscopy of Self-Assembled Monolayers on Metal Surfaces: Factor Analysis of Mixed Monolayers. *Anal. Chem.* **2019**, *91*, 1269−1276.

(67) Vericat, C.; Vela, M. E.; Salvarezza, R. C. Self-assembled monolayers of alkanethiols on Au(111): Surface structures, defects and dynamics. *Phys. Chem. Chem. Phys.* **2005**, *7*, 3258−3268.

(68) Nihonyanagi, S.; Ye, S.; Uosaki, K. Sum frequency generation study on the molecular structures at the interfaces between quartz modified with amino-terminated self-assembled monolayer and electrolyte solutions of various pH and ionic strengths. *Electrochim. Acta* **2001**, *46*, 3057−3061.

(69) Tong, Y.; Tyrode, E.; Osawa, M.; Yoshida, N.; Watanabe, T.; Nakajima, A.; Ye, S. Preferential adsorption of amino-terminated silane in a binary mixed self-assembled monolayer. *Langmuir* **2011**, *27*, 5420−5426.

(70) Garling, T.; Tong, Y.; Darwish, T. A.; Wolf, M.; Kramer Campen, R. The influence of surface potential on the optical switching of spiropyran self assembled monolayers. *J. Phys.: Condens. Matter* **2017**, *29*, 414002.

(71) Ferrer, A.; Diez-Blanco, V.; Ruiz, A.; Siegel, J.; Solis, J. Deep subsurface optical waveguides produced by direct writing with femtosecond laser pulses in fused silica and phosphate glass. *Appl. Surf. Sci.* **2007**, *254*, 1121−1125.

(72) Wang, M.; Liechti, K. M.; Wang, Q.; White, J. M. Self-assembled silane monolayers: Fabrication with nanoscale uniformity. *Langmuir* **2005**, *21*, 1848−1857.

(73) Nishi, N.; Hobara, D.; Yamamoto, M.; Kakiuchi, T. Chain-length-dependent change in the structure of self-assembled mono-layers of n-alkanethiols on Au(111) probed by broad-bandwidth sum frequency generation spectroscopy. *J. Chem. Phys.* **2003**, *118*, 1904−1911.

(74) Kett, P. J.; Casford, M. T.; Davies, P. B. Effect of multiple group orientations on sum frequency generation spectra. *Mol. Phys.* **2013**, *111*, 175−187.

(75) Thämer, M.; Garling, T.; Campen, R. K.; Wolf, M. Quantitative determination of the nonlinear bulk and surface response from alpha-quartz using phase sensitive SFG spectroscopy. *J. Chem. Phys.* **2019**, *151*, 064707.

(76) Shen, Y. R. Revisiting the basic theory of sum-frequency generation. *J. Chem. Phys.* **2020**, *153*, 180901.

(77) Yamada, C.; Kimura, T. Rotational symmetry of the surface Second-Harmonic Generation of zinc-blende-type crystals. *Phys. Rev. B* **1994**, *49*, 14372−14381.

(78) Glinka, Y. D.; Babakiray, S.; Johnson, T. A.; Holcomb, M. B.; Lederman, D. Resonance-type thickness dependence of optical second-harmonic generation in thin films of the topological insulator

B i2 S e3. *Physical Review B - Condensed Matter and Materials Physics* **2015**, *91*, 1−15.

(79) Barriga, J.; Coto, B.; Fernandez, B. Molecular dynamics study of optimal packing structure of OTS self-assembled monolayers on SiO2 surfaces. *Tribiol. Int.* **2007**, *40*, 960−966.

(80) Bart, F.; Gautier, M. A LEED study of the (0001) a-quartz surface reconstruction. *Surf. Sci.* **1994**, *311*, 671.

(81) Eder, S. D.; Fladischer, K.; Yeandel, S. R.; Lelarge, A.; Parker, S. C.; Søndergård, E.; Holst, B. A Giant Reconstruction of α-quartz (0001) Interpreted as Three Domains of Nano Dauphine Twins. *Sci. Rep.* **2015**, *5*, 1−8.

(82) Canepa, M.; Maidecchi, G.; Toccafondi, C.; Cavalleri, O.; Prato, M.; Chaudhari, V.; Esaulov, V. A. Spectroscopic ellipsometry of self assembled monolayers: Interface effects. the case of phenyl selenide SAMs on gold. *Phys. Chem. Chem. Phys.* **2013**, *15*, 11559−11565.

(83) Ogieglo, W.; Wormeester, H.; Eichhorn, K. J.; Wessling, M.; Benes, N. E. In situ ellipsometry studies on swelling of thin polymer films: A review. *Prog. Polym. Sci.* **2015**, *42*, 42.

(84) Tolles, W. M.; Nibler, J. W.; McDonald, J. R.; Harvey, A. B. A Review of the theory and Application of Coherent Anti-Stokes Raman Spectroscopy (CARS). *Appl. Spectrosc.* **1977**, *31*, 253−271.

🕮 Recommended by ACS